International Journal of Heat and Fluid Flow 31 (2010) 115–125

Contents lists available at ScienceDirect

International Journal of Heat and Fluid Flow

journal homepage: www.elsevier.com/locate/ijhff

A heat transfer model for evaporation of coalescing bubbles in micro-channel flow

L. Consolini, J.R. Thome *

Laboratoire de Transfert de Chaleur et de Masse, École Polytechnique Fédérale de Lausanne, Switzerland

ARTICLE INFO

Article history:
Received 29 April 2009
Received in revised form 7 September 2009
Accepted 21 October 2009
Available online 26 November 2009

Keywords:
Micro-channel
Flow boiling
Coalescence
Heat transfer
Model

ABSTRACT

The current study presents a one-dimensional model of confined coalescing bubble flow for the prediction of micro-channel convective boiling heat transfer. Coalescing bubble flow has recently been identified as one of the characteristic flow patterns to be found in micro-scale systems, occurring at intermediate vapor qualities between the isolated bubble and the fully annular regimes. As two or more bubbles bond under the action of inertia and surface tension, the passage frequency of the bubble–liquid slug pair declines, with a redistribution of liquid among the remaining flow structures. Assuming heat transfer to occur only by conduction through the thin evaporating liquid film trapped between the bubbles and the channel wall, the present model includes a simplified description of the dynamics of the formation and flow of the liquid film and the thin film evaporation process, taking into account the added mass transfer by breakup of the bridging liquid slugs. The new model has been confronted against experimental data taken within the coalescing bubble flow mode that have been identified by a diabatic micro-scale flow pattern map. The comparisons for three different fluids (R-134a, R-236fa and R-245fa) gave encouraging results with 83% of the database predicted within a ±30% error band. Furthermore, the new model is able to predict a "nucleate boiling curve" with an exponent of 0.74 typical of numerous micro-channel flow boiling studies, thus suggesting film evaporation as the controlling heat transfer mechanism rather than nucleate boiling.

1. Introduction

The studies that in the past decades have treated micro-channel vaporizing flows have delivered evidence, with different degrees of insight, to the characteristics of confined convective boiling in terms of heat transfer, pressure drop, flow patterns, critical heat flux, etc. Two-phase micro-channel heat transfer has been a subject of extensive investigation, and is currently in the process of being thoroughly mapped out experimentally. The evidence that is presently available has shown the sensitivity of two-phase heat transfer coefficients to parameters ranging from the applied heat flux to fluid properties. However, the pace of modeling efforts on the subject has not matched the production rate of experimental databases, and the current availability of prediction schemes is rather limited, being at least in part held back by the ongoing discussion on whether macro-scale models also apply to the micro-scale, and whether nucleate boiling plays a dominant role. Some recent reviews on the subject have been made by Thome (2006), Ribatski et al. (2006) and Bertsh et al. (2008).

Among the methods presented in the literature for two-phase micro-channel heat transfer are the correlations of Lazarek and Black (1982) and Tran et al. (1996), the empirical method of Kandlikar and Balasubramanian (2004), the adaptation of Chen's superposition model by Zhang et al. (2004) and Bertsch et al. (2009), and the slug flow phenomenological model of Thome and coworkers (Thome et al., 2004; Dupont et al., 2004). The first two methods cited are simple equations that correlate experimental data to the parameters that influenced the heat transfer behavior in the pioneering experimental studies in which heat transfer was not a function of vapor quality or mass velocity but only of heat flux. In both cases, the authors suggest nucleate boiling as the dominant heat transfer mechanism, and their correlations include primarily heat flux and fluid properties (Lazarek and Black's correlation also has a weak dependency on mass velocity). On the other hand, Kandlikar and Balasubramanian and Zhang et al., and more recently Bertsch et al., re-propose the concept developed for macro-scale channels of a duality between nucleate boiling and convective vaporization. These studies correct methods originally developed for the macro-scale by mainly modifying the adopted single-phase correlations to account for the possibility of a laminar liquid phase, assuming nucleate boiling as a dominant mechanism.

The method of Thome et al. (2004), which extended the work on micro-channel slug flow of Jacobi and Thome (2002), is a purely

* Corresponding author. Address: EPFL-STI-IGM-LTCM, Station 9, CH-1015 Lausanne, Switzerland. Tel.: +41 21 693 59 82; fax: +41 21 693 59 60.
E-mail addresses: lorconsolini@tin.it (L. Consolini), john.thome@epfl.ch (J.R. Thome).

0142-727X/$ - see front matter © 2009 Elsevier Inc. All rights reserved.
doi:10.1016/j.ijheatfluidflow.2009.10.005

Nomenclature

Latin

A	cross-sectional area, m^2
Bo	modified Boiling number, –
Bn	Bond number, –
D	diameter, m
E	total energy, J
f	bubble–liquid passage frequency, Hz
fr	Fanning friction factor, –
G	mass velocity, kg/m^2 s
h	specific enthalpy, J/kg
k	thermal conductivity, W/mK
m	mass, kg
Nu	Nusselt number, –
p	saturation pressure, Pa
q	heat flux, W/m^2
t	time, s
u	specific internal energy, J/kg
V	volume, m^3
W	mean axial velocity, m/s
x	vapor quality, –
z	axial coordinate, m

Greek

α	heat transfer coefficient, W/m^2K
β	frequency power law exponent, –
δ	liquid film thickness, m
μ	dynamic viscosity, Pa s
ψ	reduced coalescing mass flux, –
ρ	density, kg/m^3
σ	surface tension, N/m
τ	shear stress, Pa
Θ	reduced function, –
ϑ	residence time, s
ξ	liquid fraction to film, –

Subscripts

a	coalescing bubble–annular transition
CV	control volume
c	isolated bubble–coalescing bubble transition coalescence
i	liquid–vapor interface
L	liquid inventory
l	liquid
lv	liquid–vapor
max	maximum value
N	bubble nose
T	bubble tail
v	vapor
0	initial
134a	referring to R-134a at the given temperature

convective boiling model for confined slug flow. The local flow characteristics are modeled as a cyclical passage, with *constant* frequency, of a saturated liquid slug, an elongated bubble with an evaporating thin film at the heated wall, and a dry vapor zone that develops once the liquid film is depleted. The local heat transfer coefficient thus results as a time-averaged value, over the total passage period ϑ, of these successive heat transfer mechanisms:

$$\bar{\alpha} = \frac{1}{\vartheta}\left(\vartheta_{liquid}\bar{\alpha}_{liquid} + \vartheta_{film}\bar{\alpha}_{film} + \vartheta_{dry}\bar{\alpha}_{dry}\right) \quad (1)$$

where the subscripted ϑs are the respective residence times. While the first and third terms at the right of Eq. (1) represent single-phase contributions, heat transfer in the film evaporation zone is postulated as pure conduction through the film's thickness with no presence of bubble nucleation. The authors thus claimed that a slug flow heat transfer coefficient, which may have the same features as in nucleate boiling (for example, by displaying a strong heat flux dependency), is actually governed by thin film evaporation.

The passage of bubble trains, with slugs of liquid bridging neighboring bubbles, referred to by Eq. (1) and generally classified as a *slug flow*, is found at low and intermediate vapor qualities in micro-channel systems. Within this general classification, Revellin and Thome (2006), and more recently Ong and Thome (2009), segregated the flow into an *isolated bubble flow* when the formation rate of bubbles by the nucleation process is much higher than their rate of coalescence, and a *coalescing bubble flow* in the range of vapor qualities where the characteristic bubble passage frequency ($f = 1/\vartheta$) reduces from a peak value to zero (representing the transition to annular flow). Fig. 1 illustrates the micro-channel flow pattern map proposed by Revellin and Thome (2006) and recently update by Ong and Thome (2009).

During coalescence, the breakup process of the liquid slugs induces a redistribution of liquid among the remaining flow structures, including the film surrounding individual bubbles. The present study is aimed at including coalescence in the description of the thin evaporating film and thus accounting for its impact on heat transfer. As a further development to the study that culminated with Eq. (1), the current investigation therefore presents a simplified analysis of one-dimensional slug flow with bubble coalescence. Before presenting the model, the following list summarizes its main assumptions: (1) the two-phases are in thermodynamic equilibrium, with no liquid superheating, (2) the bubbles are nucleated periodically only at the origin of the heated length, where the vapor quality is $x = 0$, (3) the bubble departure from the heated wall occurs only axially, with no radial detachment, (4) the liquid film surrounding the confined bubble is laminar, with negligible inertial effects, and is driven only by interfacial shear, (5) the flow presents axial symmetry, (6) the interface of the liquid film varies linearly in the axial direction, (7) pressure drop is

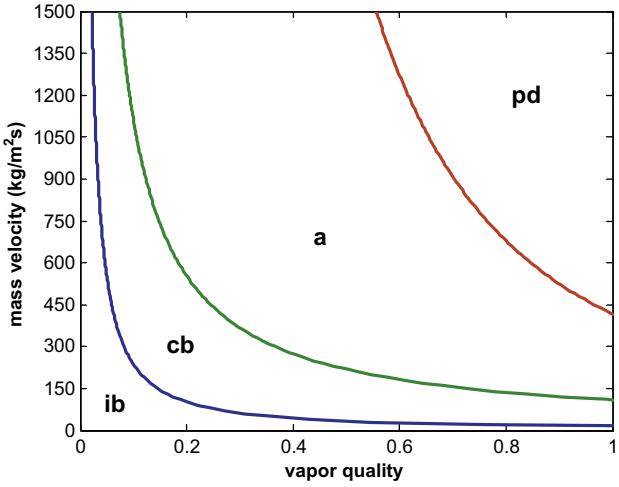

Fig. 1. The flow pattern map of Revellin and Thome (2006), updated by Ong and Thome (2009): ib – isolate bubble flow, cb – coalescing bubble flow, a – annular flow, pd – post dry-out flow. Simulated for R-134a at 7 bar with a mass velocity of 500 kg/m^2 s and a heat flux of 50 kW/m^2 in a 500 μm diameter channel.

negligible and the fluid properties are constant, (8) the liquid film thickness is small compared to the channel size, (9) the heat flux is constant and uniform, and is used only to evaporate the liquid, and (10) the heat transfer to the liquid slug and any dry patch that may occur is negligible. The above assumptions may have different impacts on the effectiveness of the model. For example, taking the bubbles to nucleate at the location where $x = 0$ may be more acceptable at higher mass velocities, when the extent of the bubbly flow regime collapses towards the saturated liquid curve, rather than at lower flow rates where nucleation may take place over a more substantial length of the heated section. Assuming axial symmetry and no radial departure of the bubble simplifies the treatment of the problem (for example, circumferential flows induced by gravity or surface tension are neglected), and applies best to high confinement number cases where this type of flow geometry is more likely. Neglecting pressure drop in assessing the dynamics of the liquid film is also arguable, particularly when the bubble experiences a high acceleration. However, recent studies have suggested that in numerous slug flow conditions, the pressure drop develops mainly within the liquid slugs rather than in the bubbles (see for example Garimella et al., 2003). On a final note, taking the liquid–vapor interface as linear should give a fairly good representation of the bubble far from the high-curvature extremities, and in the absence of interfacial waves.

2. Bubble dynamics

As a starting point for the current analysis, consider the slug flow illustrated in Fig. 2. A mass balance over the finite control volume (*CV* in Fig. 2), which presents a stationary boundary in the all-liquid flow entering the heated sector and a moving boundary (with velocity equal to the bubble nose velocity, W_N) at the nose of the unspecified bubble, yields

$$\frac{dm_{CV}}{dt} = \frac{1}{4} G \pi D^2 \tag{2}$$

where G is the total flow mass velocity, D is the channel diameter, and m_{CV} is the mass inventory of the control volume. Indicating with V_{CV} and V_v, respectively, the total volume of *CV*, and that of the vapor within it, and observing that

$$\frac{dV_{CV}}{dt} = \frac{1}{4} W_N \pi D^2 \tag{3}$$

then

$$\frac{dm_{CV}}{dt} = \rho_l \frac{dV_{CV}}{dt} - (\rho_l - \rho_v)\frac{dV_v}{dt} = \frac{1}{4}\rho_l W_N \pi D^2 - (\rho_l - \rho_v)\frac{dV_v}{dt} \tag{4}$$

Combining Eqs. (2) and (4) provides the expression for the velocity of the bubble nose as

$$W_N = \frac{G}{\rho_l} + \left(1 - \frac{\rho_v}{\rho_l}\right)\frac{4}{\pi D^2}\frac{dV_v}{dt} \tag{5}$$

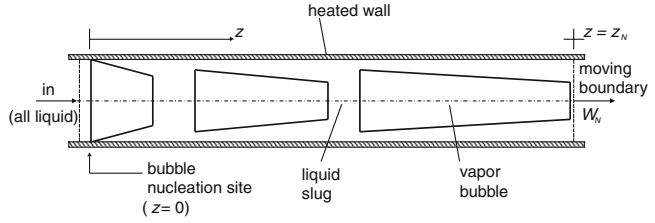

Fig. 2. The control volume for the determination of the velocity and position of the bubble nose.

which gives the slug velocity as the sum of the speed of the liquid entering the channel plus a contribution of the phase-change expansion occurring within the control volume.

Having assumed the phases to be saturated, an energy balance may be written as

$$\frac{dE_{CV}}{dt} = \frac{1}{4} G \pi D^2 h_l + \pi D q z_N - p\frac{dV_{CV}}{dt} \tag{6}$$

with h_l the saturated liquid enthalpy, q the applied heat flux, and z_N the axial position of the moving boundary (see Fig. 2). Neglecting any kinetic energy contribution, the time derivative of the total energy in the control volume is

$$\frac{dE_{CV}}{dt} = \rho_l\left[\frac{d(V_{CV}u_l)}{dt} - \frac{d(V_v u_l)}{dt}\right] + \rho_v \frac{d(V_v u_v)}{dt} \tag{7}$$

where u_l and u_v are respectively the specific internal energies of the two-phases. Applying the definition of enthalpy ($h \equiv u + p/\rho$), Eq. (7) may be expressed as

$$\frac{dE_{CV}}{dt} = \rho_l h_l \frac{dV_{CV}}{dt} - (\rho_l h_l - \rho_v h_v)\frac{dV_v}{dt} - p\frac{dV_{CV}}{dt} \tag{8}$$

From Eqs. (3), (6) and (8),

$$W_N = \frac{G}{\rho_l} + \left(1 - \frac{\rho_v h_v}{\rho_l h_l}\right)\frac{4}{\pi D^2}\frac{dV_v}{dt} + \frac{4q}{\rho_l h_l}\frac{z_N}{D} \tag{9}$$

Setting $W_N = dz_N/dt$, and combining Eqs. (5) and (9) to remove the term dV_v/dt, one obtains

$$\frac{dz_N}{dt} = \frac{G}{\rho_l} + \frac{4q}{\rho_v h_{lv}}\frac{z_N}{D} \tag{10}$$

where h_{lv} is the latent heat of vaporization ($h_{lv} \equiv h_v - h_l$), and having assumed $\rho_v \ll \rho_l$.[1] Eq. (10) represents a linear ordinary differential equation in z_N. For a time-varying heat flux, the general solution to Eq. (10) is

$$z_N(t) = \exp\left(\frac{4}{\rho_v h_{lv} D}\int q dt\right)\left[\frac{G}{\rho_l}\int \exp\left(-\frac{4}{\rho_v h_{lv} D}\int q dt\right)dt + C\right] \tag{11}$$

where C is the integration constant. On the other hand, assuming a constant q and setting the initial condition to $z_N(0) = 0$ (the bubble nose is generated at the origin of the heated length), Eq. (10) gives the following time law governing the motion of the bubble nose (or equivalently, the time law for the motion of the liquid slug traveling in front of the bubble):

$$z_N(t) = \frac{G}{\rho_l}\frac{\rho_v h_{lv} D}{4q}\left[\exp\left(\frac{4q}{\rho_v h_{lv} D}t\right) - 1\right] \tag{12}$$

3. Thin film evaporation process

Fig. 3 illustrates an elongated bubble during its flow through a heated circular channel. An analysis over the control volume in Fig. 3, positioned in the thin evaporating film surrounding the bubble, yields the following equation for conservation of mass:

$$\frac{\partial}{\partial t}\left[\frac{\delta}{D}\left(1 - \frac{\delta}{D}\right)\right] + \frac{\partial}{\partial z}\left[W\frac{\delta}{D}\left(1 - \frac{\delta}{D}\right)\right] = -\frac{1}{\rho_l D}\left(1 - 2\frac{\delta}{D}\right)\dot{m}''_{evp} \tag{13}$$

with $\dot{m}''_{evp}$ the evaporating mass flux, and W the average liquid film velocity in the z direction. In the same fashion, conservation of energy yields

[1] For cases where $\rho_v \ll \rho_l$ is not satisfied, $1/\rho_v$ appearing in the second term on the right side of Eq. (10) should be replaced by $(1/\rho_v - 1/\rho_l)$.

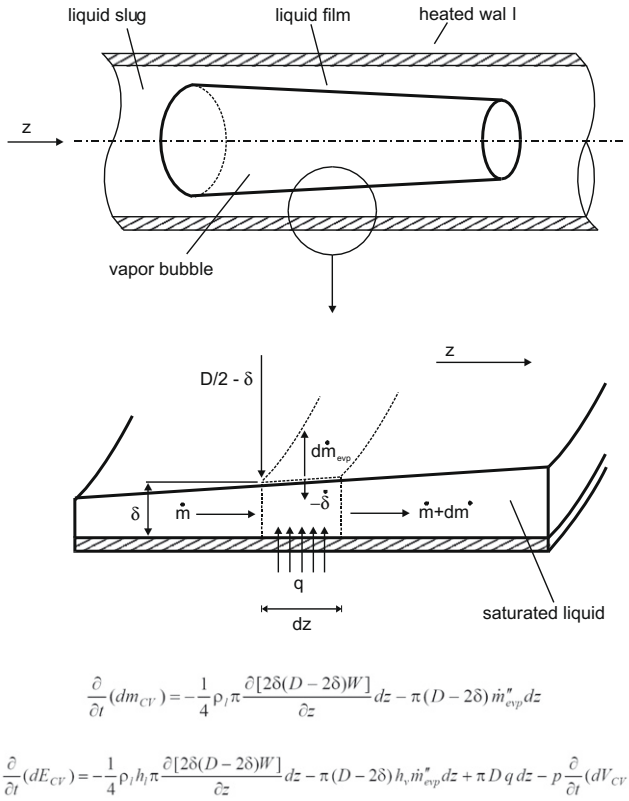

$$\frac{\partial}{\partial t}(dm_{CV}) = -\frac{1}{4}\rho_l \pi \frac{\partial[2\delta(D-2\delta)W]}{\partial z}dz - \pi(D-2\delta)\dot{m}''_{evp}dz$$

$$\frac{\partial}{\partial t}(dE_{CV}) = -\frac{1}{4}\rho_l h_l \pi \frac{\partial[2\delta(D-2\delta)W]}{\partial z}dz - \pi(D-2\delta)h_v \dot{m}''_{evp}dz + \pi D\, q\, dz - p\frac{\partial}{\partial t}(dV_{CV})$$

Fig. 3. Schematic representation of an elongated bubble, and the control volume for the analysis of the liquid film.

$$\frac{\partial}{\partial t}\left[\frac{\delta}{D}\left(1-\frac{\delta}{D}\right)\right] + \frac{\partial}{\partial z}\left[W\frac{\delta}{D}\left(1-\frac{\delta}{D}\right)\right] = -\frac{1}{\rho_l D}\frac{h_v}{h_l}\left(1-2\frac{\delta}{D}\right)\dot{m}''_{evp} + \frac{q}{\rho_l h_l D} \tag{14}$$

The governing equation for the film thickness is obtained by combining Eqs. (13) and (14):

$$\frac{\partial}{\partial t}\left[\frac{\delta}{D}\left(1-\frac{\delta}{D}\right)\right] + \frac{\partial}{\partial z}\left[W\frac{\delta}{D}\left(1-\frac{\delta}{D}\right)\right] = -\frac{q}{\rho_l h_{lv} D} \tag{15}$$

Assuming the film to be driven only by interfacial shear, τ_i, and neglecting the pressure drop and inertial terms, the mean cross-sectional velocity of the film in the axial direction is given from an axial momentum balance as

$$W = \frac{\tau_i D}{2\mu_l}\left[\frac{(1-2\frac{\delta}{D})^3}{4\frac{\delta}{D}(1-2\frac{\delta}{D})}\ln\left(1-2\frac{\delta}{D}\right) + \frac{1}{2}\left(1-2\frac{\delta}{D}\right)\right] \tag{16}$$

which, when applying the thin film approximation ($\delta/D \ll 1$), simplifies to the following asymptotic expansion

$$W \sim \frac{\tau_i D}{2\mu_l}\frac{\delta}{D} + O\left[\left(\frac{\delta}{D}\right)^2\right] \tag{17}$$

Inserting Eq. (17) into Eq. (15), and dropping the higher order terms in δ/D, yields the quasi-linear expression,

$$\frac{\partial\delta}{\partial t} + \frac{\tau_i}{\mu_l}\delta\frac{\partial\delta}{\partial z} = -\frac{q}{\rho_l h_{lv}} \tag{18}$$

By adopting the simplifying assumption of a linear variation of the film thickness with z, which is deemed acceptable far from the bubble nose and its tail, the solution to Eq. (18) may be sought by utilizing the convenient form,

$$\delta(t,z) = \delta_0(t) + z\delta_1(t) \tag{19}$$

where δ_0 and δ_1 are two unknown functions of time. Inserting Eq. (19) into Eq. (18) gives

$$\left(\frac{d\delta_0}{dt} + \frac{\tau_i}{\mu_l}\delta_1\delta_0\right) + z\left(\frac{d\delta_1}{dt} + \frac{\tau_i}{\mu_l}\delta_1^2\right) = -\frac{q}{\rho_l h_{lv}} \tag{20}$$

Confronting the two sides of Eq. (20) yields the following system of ordinary differential equations,

$$\frac{d\delta_0}{dt} + \frac{\tau_i}{\mu_l}\delta_1\delta_0 = -\frac{q}{\rho_l h_{lv}} \tag{21}$$

$$\frac{d\delta_1}{dt} + \frac{\tau_i}{\mu_l}\delta_1^2 = 0 \tag{22}$$

whose solution for δ_0 is

$$\delta_0(t) = \frac{1}{t+C_1}\left[C_0 - \frac{1}{\rho_l h_{lv}}\int (t+C_1)q\,dt\right] \tag{23}$$

while for δ_1,

$$\delta_1(t) = \frac{\mu_l}{\tau_i(t+C_1)} \tag{24}$$

C_0 and C_1 are the two constants of integration. Therefore, Eqs. (19), (23) and (24) give the governing equation for the local film thickness as

$$\delta(t,z) = \frac{\frac{\mu_l}{\tau_i}z + C_0}{t+C_1} - \frac{1}{\rho_l h_{lv}}\frac{\int(t+C_1)q\,dt}{t+C_1} \tag{25}$$

When the heat flux is constant, Eq. (25) becomes

$$\delta(t,z) = \frac{\frac{\mu_l}{\tau_i}z + C_0}{t+C_1} - \frac{q}{2\rho_l h_{lv}}(t+C_1) \tag{26}$$

4. Initial and boundary conditions for the film thickness equation

In the context of an evaporating elongated bubble, Eqs. (25) and (26) represent the behavior of the liquid film deposited by a liquid slug during its passage through the channel. In order to make use of either equation, initial and boundary conditions must be assigned in order to determine the values of C_0 and C_1. Referring to the constant heat flux case Eq. (26), assuming that a bubble nucleates at $t = 0$ and at the origin of the heated length, $z = 0$, no liquid–vapor interface should exist for $t \to 0$ over $z > 0$. Thus, for $z > 0$,

$$\lim_{t\to 0}\delta(t,z) = +\infty \tag{27}$$

Eq. (27) implies that the bubble does not exist at a time that approaches the instant in which nucleation begins, and this is satisfied when $C_1 = 0$ and $C_0 \geqslant 0$.

As for the boundary condition at $z = 0$, i.e. $\delta(t,0) = \delta^{(0)}(t)$, the assumption that the bubble detachment process occurs only axially and not in the radial direction yields $\delta^{(0)}(t) \leqslant 0$. In other words, $z = 0$ represents either a contact location of the bubble with the channel wall, or a dry perimeter (a negative $\delta^{(0)}$ implies a local condition of film dry-out). From Eq. (26), having set $C_1 = 0$,

$$\delta^{(0)}(t) = \frac{C_0}{t} - \frac{q}{2\rho_l h_{lv}}t \leqslant 0 \tag{28}$$

The above inequality will be satisfied only when $C_0 = 0$, and thus Eq. (26) now yields

$$\delta(t,z) = \frac{\mu_l}{\tau_i}\frac{z}{t} - \frac{q}{2\rho_l h_{lv}}t \tag{29}$$

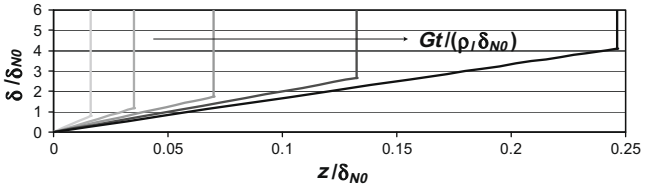

Fig. 4. Temporal evolution of the liquid film and the bubble nose at the initial stages of the bubble development [$\delta_{N0}/D = 0.02$ and $q/(Gh_{lv}) = 6.0 \times 10^{-4}$].

Fig. 4 shows the temporal evolution of the film thickness and the bubble nose (the vertical segments in Fig. 4) at the early stages of their development.[2] Locally, the film shrinks in time due to the combined effect of the vaporization process and the drag exerted by the vapor phase.

Inserting Eq. (12) into Eq. (29) gives the time law of the nose film thickness,

$$\delta_N(t) = \frac{G\mu_l}{\rho_l \tau_i}\frac{\rho_v h_{lv} D}{4q}\left[\frac{\exp\left(\frac{4q}{\rho_v h_{lv} D}t\right)-1}{t}\right] - \frac{q}{2\rho_l h_{lv}}t \tag{30}$$

The initial film thickness results from taking the limit for $t \to 0$ of Eq. (30),

$$\delta_{N0} \equiv \lim_{t\to 0}\delta_N(t) = \frac{G\mu_l}{\rho_l \tau_i} \tag{31}$$

The value from Eq. (31) represents the nose film thickness at the instant the bubble forms (see Fig. 4).

For the adiabatic case, the limit of Eq. (30) for $q \to 0$ yields $\delta_{N,adiabatic} = \delta_{N0}$ (assuming that the interfacial shear for an adiabatic flow is approximately equal to that of a diabatic flow: $\tau_{i,adiabatic} \approx \tau_{i,diabatic}$); that is, the bubble's nose film thickness remains unchanged in adiabatic flows. Rearranging Eqs. (29) and (31), and utilizing the inverse of Eq. (12), gives the non-dimensional film thickness of the bubble nose, δ_N/D, as

$$\frac{\delta_N}{D} = \frac{\left(\frac{\rho_l W_N}{G}-1\right)\frac{\delta_{N0}}{D}}{\ln\left(\frac{\rho_l W_N}{G}\right)} - \frac{1}{8}\frac{\rho_v}{\rho_l}\ln\left(\frac{\rho_l W_N}{G}\right) \tag{32}$$

The value of δ_{N0}/D is the non-dimensional nose film thickness for an adiabatic flow; that is, when the bubble nose speed is equal to $W_{N0} = G/\rho_l$ in the thin film approximation see Eq. (10). Fig. 5a illustrates the predicted nose film thicknesses by what is referred to as Taylor's law, which was developed under adiabatic conditions for highly viscous fluids, and states that the non-dimensional nose film thickness is only a function of the bubble's capillary number, $Ca_0 \equiv \mu_l W_{N0}/\sigma$:

$$\frac{\delta_{N0}}{D} = \frac{0.67 Ca_0^{2/3}}{1 + 2.5 \times 1.34 Ca_0^{2/3}} \tag{33}$$

(recently Han and Shikazono (2009), have extended Taylor's law to include effects of the bubble Reynolds and Weber numbers). Fig. 5b shows the predictions of Eq. (32), plotted versus the non-dimensional velocity $\rho_l W_N/G$, utilizing Eq. (33) for δ_{N0}/D. As the value of Ca_0 increases (higher mass velocity), the initial film thickness increases and causes a rise in the diabatic nose film thickness δ_N/D. Furthermore, as the vaporization process makes the bubble faster, its nose film thickness again rises.

This increase in δ_N/D is thus also consistent with the adiabatic trend given by Eq. (33), and agrees with the scenario suggested

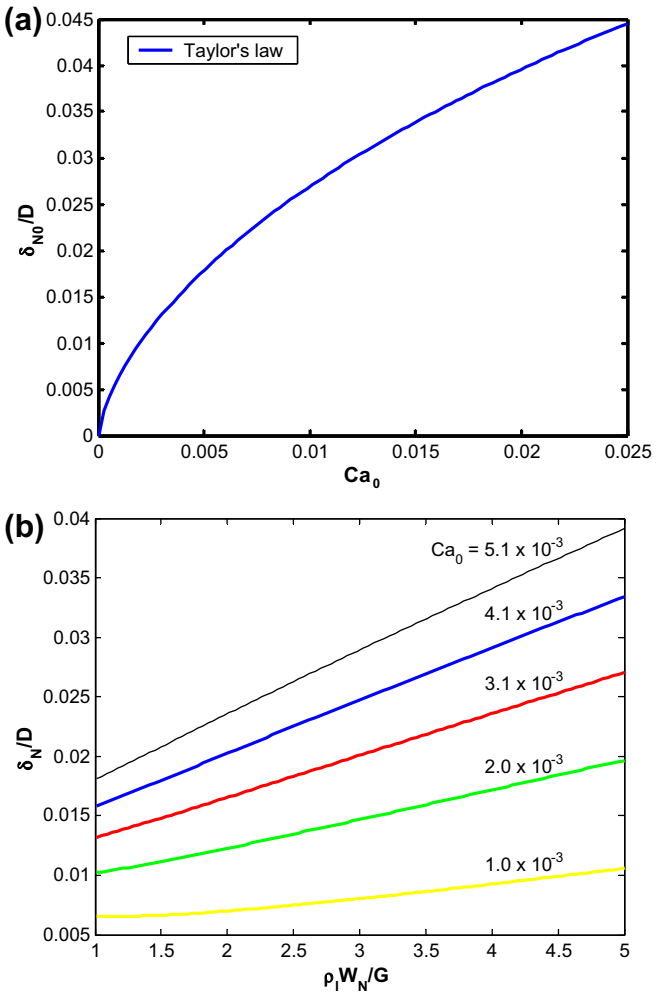

Fig. 5. (a) Taylor's law versus the adiabatic capillary number, and (b) the non-dimensional nose film thickness plotted versus the non-dimensional bubble velocity, at different values of Ca_0 ($\rho_l/\rho_v = 67$).

by Moriyama and Inoue (1996) for slow bubbles that have values of the Bond number $Bn \equiv \rho_l \dot{W}_N^2 D/\sigma$ less than 2. In this case, the liquid film is thinner than the boundary layer in the liquid slug, and δ_N increases with bubble nose speed. On the other hand, Moriyama and Inoue also postulated that for $Bn > 2$, the film scales with the thickness of the boundary layer, and higher velocities deliver thinner liquid films. However, to capture both mechanisms may require relaxing the thin film approximation in deriving Eq. (10), while developing a suitable correspondence between interfacial shear and the shear in the liquid slugs.

5. Bubble frequency and coalescence

Experimental observations have shown that the bubble–slug passage has a cyclical nature. However, beyond a certain threshold vapor quality, the passage frequency falls sharply due to the rapid increase of coalescence among nearby bubbles (refer for example to Revellin et al., 2006, 2008). In general terms, the frequency presents a maximum value, f_{max}, at the transition vapor quality between the isolate bubble and coalescing bubble flow modes, and declines to zero at the transition to annular flow, as shown in Fig. 6a. Denoting with x_c and x_a these two transition vapor qualities (see Figs. and 6a), the frequency function may be expressed as (Fig. 6b)

$$\frac{f}{f_{max}} = \left(\frac{x_a - x}{x_a - x_c}\right)^{\beta} \tag{34}$$

[2] Fig. 4 is expressed in terms of the reduced quantities $\delta^+ = \delta_N/\delta_{N0}$, $z^+ = z/\delta_{N0}$, and $t^+ = Gt/(\delta_{N0}\rho_l)$, where $\delta_{N0} \equiv G\mu_l/(\rho_l \tau_i)$ see Eq. (31). Utilizing these three non-dimensional parameters, Eq. (29) may be rewritten as $\delta^+ = (z^+/t^+) - qt^+/(2Gh_{lv})$.

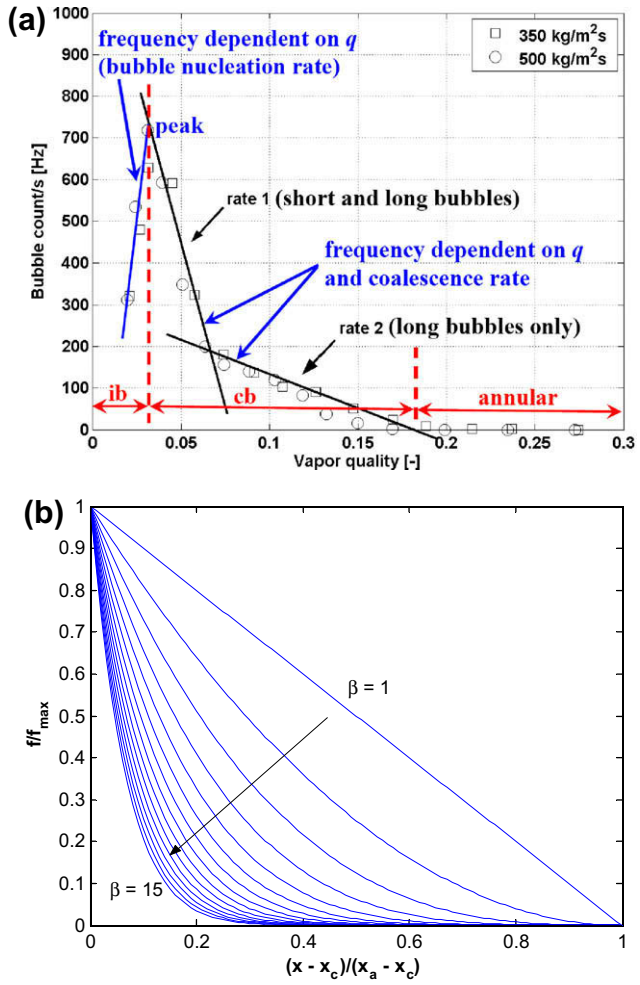

Fig. 6. (a) Experimental bubble passage frequency versus exit vapor quality for a two-phase flow of R-134a at 30 °C in a uniformly heated 510 μm circular microchannel. Data shown for 350 and 500 kg/m² s. (b) Eq. (34) plotted for β from 1 to 15.

where $\beta \geqslant 1$ is a generic shape factor.

A change in the mass of liquid of a bubble–slug pair during its travel through a heated channel is due (i) to a variation of the vapor quality from the heating process and (ii) to a change in frequency associated, for instance, to coalescence. Defining the cyclical passage of liquid in terms of vapor quality, x, and local frequency, f, the amount of liquid mass crossing a given location over one passage period is $m_L = G\pi D^2(1-x)/(4f)$. The mass variation due to a unitary change in frequency will then be

$$\frac{\partial m_L}{\partial f} = -\frac{G\pi D^2(1-x)}{4f^2} \tag{35}$$

When multiplied by the elementary change in frequency, df, Eq. (35) serves as an estimate of the mass of liquid redistributed to the bubble–slug pair during coalescence (Fig. 7). A fraction of this added mass will be distributed to the liquid slug, while the remaining fraction, ξ (<1), will participate in the film evaporation process (as a first approximation, ξ is taken to be constant). Treating this liquid intake by the film as an incoming liquid flux, $\dot{m}_c''$, and assuming the residence time of the liquid slug to be negligible with respect to that of the bubble,[3] the incremental mass added to the liquid film owing to a change in frequency, df, will be

[3] The ratio of the residence time of the liquid slug to that of the bubble is approximately equal to $\rho_l(1-x)/(\rho_l x)$. For a density ratio of 100 and a vapor quality of 0.15, the residence time of the liquid slug is only 6% that of the bubble.

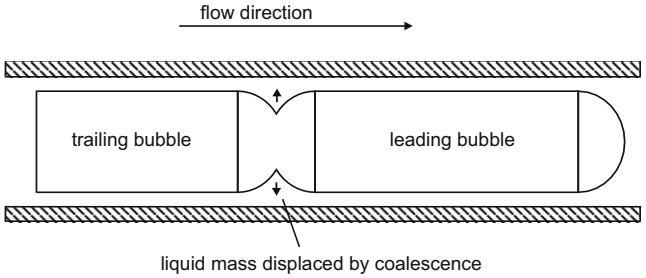

Fig. 7. Schematic diagram of coalescence of two bubbles.

$$dm_c = \frac{\dot{m}_c'' \pi D dz}{f} = \xi \frac{\partial m_L}{\partial f} df \tag{36}$$

In view of Eqs. (34)–(36), and utilizing the expression for the vapor quality gradient, $dx/dz = 4q/(Gh_{lv}D)$, the mass flux in Eq. (36) may be expressed as

$$\dot{m}_c''(x) = \frac{q}{h_{lv}} \psi(x) \tag{37}$$

where the function Ψ is

$$\psi(x) \equiv \xi\beta\left(\frac{1-x}{x_a - x}\right) \tag{38}$$

The incoming mass of liquid given by Eq. (37) is accounted for by modifying Eq. (18) to

$$\frac{\partial \delta}{\partial t} + \frac{\tau_i}{\mu_l}\delta\frac{\partial \delta}{\partial z} = -\frac{q}{\rho_l h_{lv}}[1 - \psi(x(z))] \tag{39}$$

In order to obtain a closed-form solution for the film thickness, the expansion

$$\psi(x) \sim \psi(x_c) + O(x - x_c) \tag{40}$$

allows replacing $\psi(x)$ with $\psi(x_c)$ in the neighborhood of x_c, reducing Eq. (39) to

$$\frac{\partial \delta}{\partial t} + \frac{\tau_i}{\mu_l}\delta\frac{\partial \delta}{\partial z} = -\frac{q}{\rho_l h_{lv}}(1 - \psi_c) \tag{41}$$

where

$$\psi_c \equiv \psi(x_c) = \xi\beta\left(\frac{1-x_c}{x_a - x_c}\right) \tag{42}$$

For the constant heat flux case, and by analogy to Eq. (26), the new film thickness equation is

$$\delta(t,z) = \frac{\frac{\mu_l}{\tau_i}z + C_0}{t + C_1} - \frac{q}{2\rho_l h_{lv}}(1 - \psi_c)(t + C_1) \tag{43}$$

To assure continuity between Eqs. (29) and (43) at the instant in which coalescence starts, i.e. at $t = t_c$, the values of the constants must satisfy the following conditions:

$$C_0 = -\frac{q\psi_c}{2\rho_l h_{lv}} t_c^2 \quad \text{and} \quad C_1 = 0 \tag{44}$$

Bearing this in mind, Eq. (43) becomes

$$\delta(t,z) = \frac{\mu_l}{\tau_i}\frac{z}{t} - \frac{q}{2\rho_l h_{lv}} t\left[1 - \psi_c\left(\frac{t^2 - t_c^2}{t^2}\right)\right] \tag{45}$$

which is valid for $t \geqslant t_c$. The expression for t_c is taken as the time at which the bubble nose reaches the coalescing bubble mode boundary, defined at the vapor quality $x = x_c$. Inverting Eq. (12) and substituting the expression for vapor quality, $x = 4qz/(Gh_{lv}D)$, yields

$$t_c = \frac{\rho_v h_{lv} D}{4q} \ln\left(1 + \frac{\rho_l}{\rho_v} x_c\right) \tag{46}$$

The value of the film thickness may also be expressed in terms of the local vapor quality by replacing z with $Gh_{lv}Dx/(4q)$ in Eq. (45), i.e.

$$\hat{\delta}(t,x) = \frac{\mu_l}{\tau_i}\frac{Gh_{lv}D}{4q}\frac{x}{t} - \frac{q}{2\rho_l h_{lv}} t\left[1 - \psi_c\left(\frac{t^2 - t_c^2}{t^2}\right)\right] \tag{47}$$

By applying Eq. (47), and utilizing Eqs. (12), (33) and (34), the liquid film thickness at the bubble nose may be expressed as

$$\frac{\delta_N}{D} = \frac{\delta_{N0}}{D}\frac{\rho_l}{\rho_v}\frac{x}{\ln\left(1+\frac{\rho_l}{\rho_v}x\right)} - \frac{1}{8}\frac{\rho_v}{\rho_l}\ln\left(1+\frac{\rho_l}{\rho_v}x\right)\left[1 - \psi_c + \psi_c\frac{\ln^2\left(1+\frac{\rho_l}{\rho_v}x_c\right)}{\ln^2\left(1+\frac{\rho_l}{\rho_v}x\right)}\right] \tag{48}$$

while for the tail of the bubble,

$$\frac{\delta_T}{D} = \frac{\delta_{N0}}{D}\frac{\rho_l}{\rho_v}\frac{x}{\ln\left(1+\frac{\rho_l}{\rho_v}x\right) + 4Bo\left(\frac{x_a - x_c}{x_a - x}\right)^{\beta}} - \frac{1}{8}\frac{\rho_v}{\rho_l}\left[\ln\left(1+\frac{\rho_l}{\rho_v}x\right) + 4Bo\left(\frac{x_a - x_c}{x_a - x}\right)^{\beta}\right] \times \left\{1 - \psi_c + \psi_c\frac{\ln^2\left(1+\frac{\rho_l}{\rho_v}x_c\right)}{\left[\ln\left(1+\frac{\rho_l}{\rho_v}x\right) + 4Bo\left(\frac{x_a - x_c}{x_a - x}\right)^{\beta}\right]^2}\right\} \tag{49}$$

where Bo is the modified Boiling number, $Bo \equiv q/(\rho_v h_{lv} D f_{max})$.

Keeping in mind the level of approximation adopted in deriving the expression for the liquid film thickness, with special reference to the replacement of Eq. (39) with Eq. (41), Eq. (49) provides an interesting element of discussion concerning the liquid film. Taking the limit of Eq. (49) for $x \to x_a$ yields (see Fig. 8a),

$$\lim_{x \to x_a} \frac{\delta_T}{D}(x;\psi_c) = \begin{cases} +\infty & \psi_c > 1 \\ 0 & \psi_c = 1 \\ -\infty & \psi_c < 1 \end{cases} \tag{50}$$

Eq. (50) provides three different scenarios according to the value of the non-dimensional mass flux, ψ_c: (1) if the flow conditions are such that ψ_c is greater than unity, liquid mass accumulates in the film, destabilizing it; (2) when ψ_c is equal to 1, the film is stable in the entire range of vapor qualities, $x_c < x \leqslant x_a$, and the flow is at a threshold; (3) for flows such that ψ_c is less than 1, the liquid film remains stable although tail dry-out occurs, and a trailing dry zone follows the bubble in its passage through the heated length (this is similar to the flow considered in Thome et al. (2004)). The two latter cases yield stable bubbles, with bounded films that run dry as the flow approaches $x = x_a$ and as the residence time tends to infinity, $1/f \to \infty$ (see the two δ_T curves in Fig. 8a for $\psi_c = 0.5$ and 1). When $\psi_c > 1$ the liquid film is unbounded, and this is the only case in Eq. (50) where there is no chance of liquid depletion as the flow approaches the annular flow transition. Eq. (50) therefore hints to the conclusion that (i) when $\psi_c \leqslant 1$, a coalescing bubble flow persists all the way to $x = x_a$, where the film vanishes and thus x_a is equal to 1 or is undefined while (ii) when $\psi_c > 1$ the film is unstable and $x_a < 1$ (see Fig. 8b). In other terms, Eq. (42) and Eq. (50) yield the following: $\xi > \xi_a$ when $x_c < x_a < 1$, where ξ_a is defined as

$$\xi_a \equiv \frac{1}{\beta}\left(\frac{x_a - x_c}{1 - x_c}\right) \tag{51}$$

which establishes a connection between the characteristics of bubble coalescence and the flow pattern transition phenomenon.

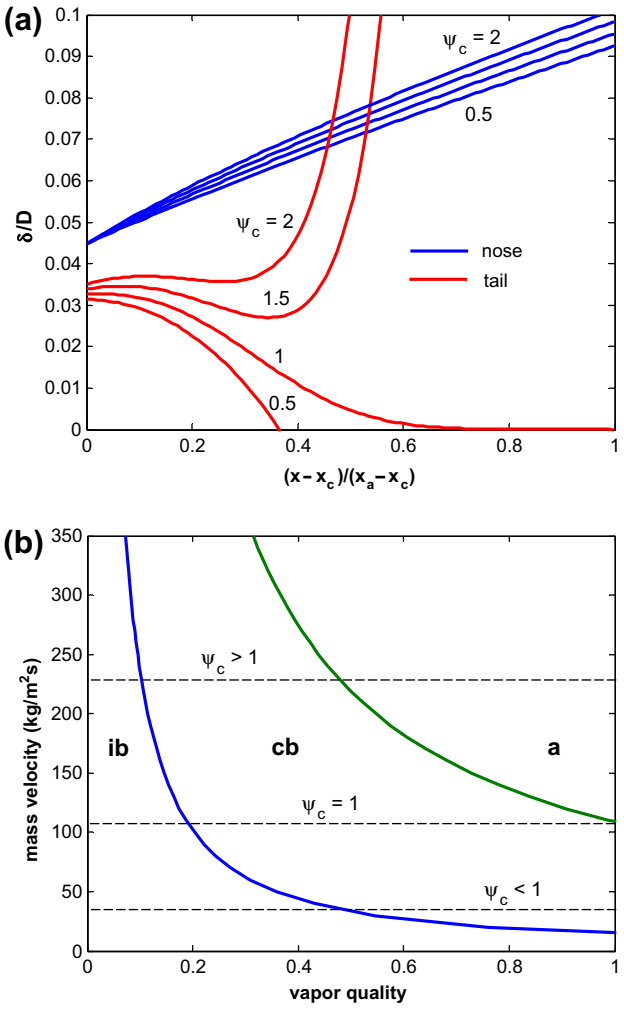

Fig. 8. (a) Non-dimensional bubble nose and tail film thicknesses versus reduced vapor quality for $\delta_{N0}/D = 0.02$, $GD/\mu_l = 1310$, $G^2D/(\rho_l\sigma) = 13.0$, $q/(Gh_{lv}) = 6.0 \times 10^{-4}$, $\beta = 6$, and ψ_c from 0.5 to 2, and (b) three paths on a micro-channel flow pattern map for different values of ψ_c (ib – isolate bubble flow, cb – coalescing bubble flow, a – annular flow).

6. Local heat transfer coefficients with a constant heat flux

Assuming pure conductive heat transfer through the laminar film of liquid surrounding the elongated bubbles, and neglecting the residence time of the liquid slug with respect to that of the bubble as noted before, the local time-averaged heat transfer coefficient may be estimated as

$$\bar{\alpha}(x) = f\int_{1/f} \frac{k_l}{\hat{\delta}(t,x)}\,dt \tag{52}$$

Performing the integration in Eq. (52), utilizing Eqs. (12), (34), (46) and (47), gives the following expression for the local time-averaged heat transfer coefficient ($\psi_c \neq 1$):

$$\bar{\alpha}(x) = \frac{k_l}{D}\frac{\left(\frac{\rho_l}{\rho_v}\right)\left(\frac{x_a - x}{x_a - x_c}\right)^{\beta}\ln\left(\frac{1-\Theta_1(x)}{1-\Theta_2(x)}\right)}{Bo(1-\psi_c)} \tag{53}$$

where the functions Θ_1 and Θ_2 are defined as

$$\Theta_1(x) \equiv \frac{(1-\psi_c)\ln^2\left(1+\frac{\rho_l}{\rho_v}x\right)}{\Theta_3(x)} \tag{54}$$

$$\Theta_2(x) \equiv \frac{(1-\psi_c)\left[\ln\left(1+\frac{\rho_l}{\rho_v}x\right)+4Bo\left(\frac{x_a-x}{x_a-x_c}\right)^{-\beta}\right]^2}{\Theta_3(x)} \tag{55}$$

with

$$\Theta_3(x) \equiv 8\frac{\mu_l}{\tau_i}\frac{G}{\rho_v D}\frac{\rho_l}{\rho_v}x - \psi_c \ln^2\left(1+\frac{\rho_l}{\rho_v}x_c\right) \tag{56}$$

Eq. (53) applies to the range of vapor quality close enough to x_c such that the replacement of $\psi(x)$ with ψ_c in Eq. (39) is acceptable. Generally, this range stretches with increasing values of x_a and decreasing values of x_c. From an operative point of view, however, it is essential to have an equation for all vapor qualities, from x_c to x_a. From this standpoint, Eq. (53) may provide an initial form for the expression of the heat transfer coefficient, which should be judiciously corrected to represent the trends in the physical data as the coalescing bubble flow regime approaches annular flow.

7. Correcting the expression for the heat transfer coefficient

Eq. (53) represents a model for the more general form of the equation for the two-phase heat transfer coefficient in the range $x_c \leqslant x < x_a$, which points out the functional dependencies of the two-phase Nusselt number, Nu,

$$\bar{\alpha}(x) = \frac{k_l}{D}Nu\left[x; x_c, x_a, \left(\frac{x_a-x}{x_a-x_c}\right)^{\beta}, \frac{\rho_l}{\rho_v}, Bo, \psi_c, \frac{\tau_i \rho_v D}{G\mu_l}\right] \tag{57}$$

Nu should be chosen to deliver the same behavior in the neighborhood of x_c as given by Eq. (53), while also correcting Eq. (53)'s prediction at the annular flow transition. For a given set of operating conditions and fluid, Nu may be taken as:

$$Nu(x) = \frac{\left(\frac{\rho_l}{\rho_v}\right)\left[\left(\frac{x_a-x}{x_a-x_c}\right)^{\beta}\right]^{\gamma(x;x_c,x_a)}\ln\left(\frac{1-\Theta_{1c}}{1-\Theta_{2c}}\right)}{Bo(1-\psi_c)} \tag{58}$$

where $\Theta_{1c} \equiv \Theta_1(x_c)$ and $\Theta_{2c} \equiv \Theta_2(x_c)$ [evaluated using Eqs. (54) and (55)], γ is a function of the local vapor quality and the coalescing bubble flow pattern boundaries, and ψ_c is calculated using Eq. (42). Utilizing Eq. (58), Eq. (57) becomes

$$\bar{\alpha}(x) = \frac{k_l}{D}\frac{\left(\frac{\rho_l}{\rho_v}\right)\left[\left(\frac{x_a-x}{x_a-x_c}\right)^{\beta}\right]^{\gamma(x;x_c,x_a)}\ln\left(\frac{1-\Theta_{1c}}{1-\Theta_{2c}}\right)}{Bo(1-\psi_c)} \tag{59}$$

γ is taken as a power law function of the vapor quality such that $\gamma = 1$ when $x = x_c$,

$$\gamma(x; x_c, x_a) = \left(\frac{x_a-x}{x_a-x_c}\right)^{\chi} \tag{60}$$

where χ is an empirical constant.

In the development of Eqs. (53) and (59), five parameters have been introduced that remain unknown and that must be defined in order to close the model: τ_i, f_{max}, β, ξ and χ. Most of these are physical quantities whose values may be estimated from either direct or indirect measurements. As was previously mentioned, the interfacial shear, τ_i, is directly related to the initial film thickness, δ_{N0} see Eq. (31). Confronting the prediction of Eq. (59) with a database of two-phase heat transfer coefficients (see Consolini and Thome, 2009), selected within the coalescing bubble flow mode (i.e. $x_c \leqslant x < x_a$), an empirical correlation was sought for τ_i of the form:

$$\tau_i = (fr_q + fr_v)\frac{G^2 x_c^2}{2\rho_v} \tag{61}$$

where fr_v is the Blasius single-phase vapor friction factor based on the Reynolds number, Gx_cD/μ_v, while fr_q is an added term that accounts for the fact that the flow is evaporating. The values for fr_q are thus correlated here as

$$fr_q = 304\left(\frac{GD}{\mu_l}\right)^{-1.16}\left(\frac{\rho_l}{\rho_v}\right)^{1.74}\left(\frac{\mu_l}{\mu_v}\right)^{1.43}x_c^{-2}\left[1-\exp\left(-\frac{qD}{h_{lv}\mu_l}\right)\right] \tag{62}$$

Note that $fr_q = 0$ when $q = 0$, and the approximation that $\tau_{i,adiabatic} \approx \tau_{i,diabatic}$ has a limited applicability.

As for the other parameters, the reported measurements of the maximum frequency, f_{max}, show its dependency on the level of heat flux, and on the fluid physical properties (see Dupont et al., 2004). Channel size, which influences the degree of bubble confinement, is also expected to play a role in defining f_{max}. Including these parameters in a dimensional analysis gives the following form:

$$\Psi\left(\frac{f_{max}\sigma}{q}, \frac{\sigma^3}{q^2 D^3 \rho_v}\right) = 0 \tag{63}$$

that has been correlated as

$$f_{max} = 0.004\left(\frac{q}{\sigma}\right)\left(\frac{\sigma^3}{q^2 D^3 \rho_v}\right)^{0.25} \tag{64}$$

As previously stated in introducing Eq. (34), β describes the decline in frequency from its peak value to zero at the transition to annular flow. The best fitting value of β to the current heat transfer database is $\beta = 1$, yielding a linear decline in frequency with vapor quality. Nonetheless, the accuracy of this conclusion should be further verified since some of the experimental trends report values of f that change with higher order power laws of x (see Revellin et al., 2006). Of the two remaining parameters, χ is entirely empirical, while ξ is a physical quantity that, however, must be deduced indirectly. Their proposed values are: $\xi = 0.02$ and $\chi = 3$.

The flow pattern boundaries of Ong and Thome (2009), which are shown in Fig. 1, are expressed by the following correlations:

$$x_c = 0.763\left(\frac{q\rho_v\sigma}{\mu_l h_{lv} G^2}\right)^{0.39} \tag{65}$$

and

$$x_a = 4.1\times 10^{-4}\left(\frac{p}{p_{134a}}\right)^{0.45}\left(\frac{GD}{\mu_l}\right)^{1.47}\left(\frac{G^2 D}{\rho_l \sigma}\right)^{-1.23} \tag{66}$$

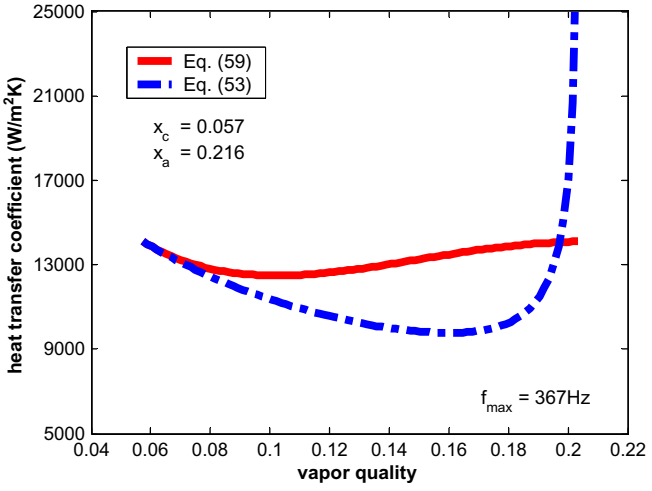

Fig. 9. Predictions from Eqs. (53) and (59) for the flow boiling heat transfer coefficients of R-134a at 31 °C in a 500 μm micro-channel at a heat flux of 50 kW/m² and mass velocity of 500 kg/m² s.

Table 1
The experimental values of the main non-dimensional parameters.

ρ_l/ρ_v	μ_l/μ_v	GD/μ_l	$qD/(h_{lv}\mu_l)$	$G^2D/(\rho_l\sigma)$	$\sigma^3/(q^2D^3\rho_v)\times 10^5$	$q\rho_v\sigma/(\mu_l h_{lv}G^2)$
27–126	14–36	385–5723	0.03–3.50	2.3–244	≈0–9.5	≈0–0.18

Fig. 9 illustrates the predicted trends in the heat transfer coefficient for a flow of R-134a as given by Eqs. (53) and (59) within the range $x_c \leqslant x < x_a$. The two solutions have the same starting value and both exhibit a decline with vapor quality in the neighborhood of x_c, which associates to an average thickening of the liquid film due to the combined effect of the film's dynamics and the mass displaced by coalescence (see Fig. 8a). The reduction of the heat transfer coefficient with increasing x is more pronounced in the case of the analytical solution Eq. (53) at the intermediate vapor qualities, while at the border to annular flow its value rises indefinitely due to the acute reduction in the film thickness by evaporation, which will lead to film dry-out. This last behavior though is not verified experimentally and thus suggests the better solution is given by Eq. (59). Both equations present minimum values of the heat transfer coefficient at the limit between a region where coalescence and film dynamics give thicker films (lower $\bar{\alpha}$), and one where film depletion by evaporation and shear either dominates or balances the coalescing mass flow (thinner film, higher $\bar{\alpha}$).

8. Heat transfer model validation and predictions

Eq. (59) was confronted with a database of 980 experimental data points in the coalescing bubble flow mode, as identified by Eqs. (65) and (66). The database included heat transfer coefficients for refrigerants R-134a, R-236fa and R-245fa in single circular channel evaporators with diameters of 510 and 790 μm, for saturation temperatures of 30–32 °C, mass velocities from 300 to 2000 kg/m^2 s, and heat fluxes up to 200 kW/m^2; see Consolini and Thome (2009) for further details on the experimental procedures and Table 1 for the ranges of the main non-dimensional groups. As shown in Fig. 10, Eq. (59) exhibits an overall success ratio of 83% of the data predicted within the ±30% error band. The best performance is for R-134a (the highest pressure refrigerant among the three) with 93% of the data inside the same error band, while the fraction of predicted data for the two other fluids drops respectively to 79% for R-236fa and 75% for R-245fa. For the same set of measurements, the model of Thome et al. (2004) predicted 75% of the data within the ±30% error band (respectively, 83% for R-134a, 56% for R-236fa and 87% for R-245fa). As can be noted in Fig. 10, the largest errors are in the vicinity of the $x = x_c$ boundary. For comparison purposes, the new Chen-type flow boiling method for micro-channels of Bertsh et al. (2009) captures only 39% of this database within ±30%.

Figs. 11–14 compare individual sets of data to the predictions of Eq. (59). Fig. 11 shows predicted and experimental heat transfer coefficients when varying the saturation temperature, and thus the fluid properties. As the fluid temperature increases, both computed and experimental values exhibit a rise that results from an overwhelming effect of a higher non-dimensional shear see Eqs. (57) and (59), $\tau_i\rho_v D/(G\mu_l)$. Fig. 11b confronts the predicted heat transfer coefficients with the measured values for the three different fluids at similar experimental conditions.

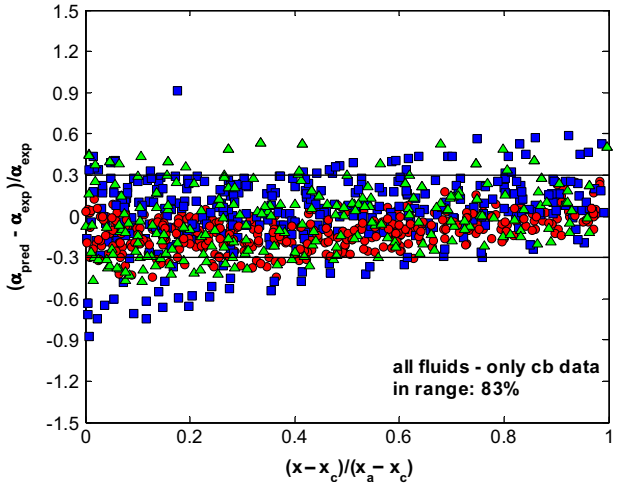

Fig. 10. The overall comparison of the predicted heat transfer coefficients by Eq. (59) with coalescing bubble (cb) data from Consolini and Thome (2009). Circle: R-134a, square: R-236fa, triangle: R-245fa.

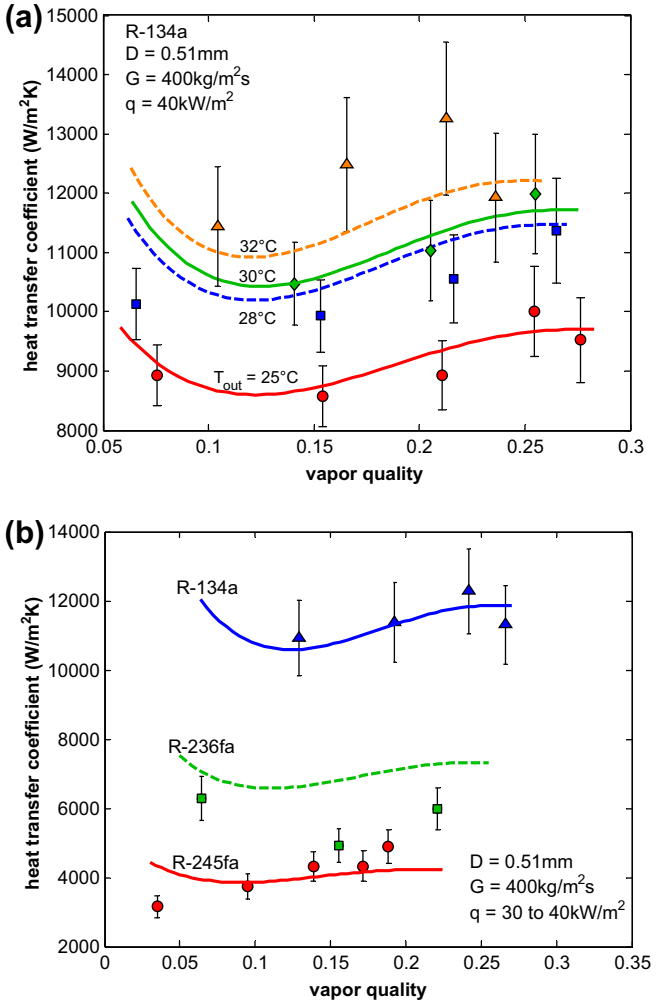

Fig. 11. (a) Experimental heat transfer coefficients versus the predictions of Eq. (59) for a flow of R-134a at different saturation temperatures (triangle: 32 °C, diamond: 30 °C, square: 28 °C, circle: 25 °C), and (b) experimental versus predicted data for R-134a (triangle), R-236fa (square) and R-245fa (circle).

The non-dimensional shear comes again into play when varying the applied heat flux. In this case, as the heat flux is increased, both $\tau_i \rho_v D/(G\mu_l)$ and Bo increase (note that in the expression for Bo also the peak frequency, f_{max}, increases, as $q^{0.5}$) yielding thinner liquid films and therefore better heat transfer, as shown in Fig. 12. The computed boiling curve in Fig. 12b ($\alpha = 2.90q^{0.74}$) has a similar proportionality to heat flux as the common nucleate boiling curve ($\alpha \propto q^{0.7}$), although in this case the results are exclusively due to

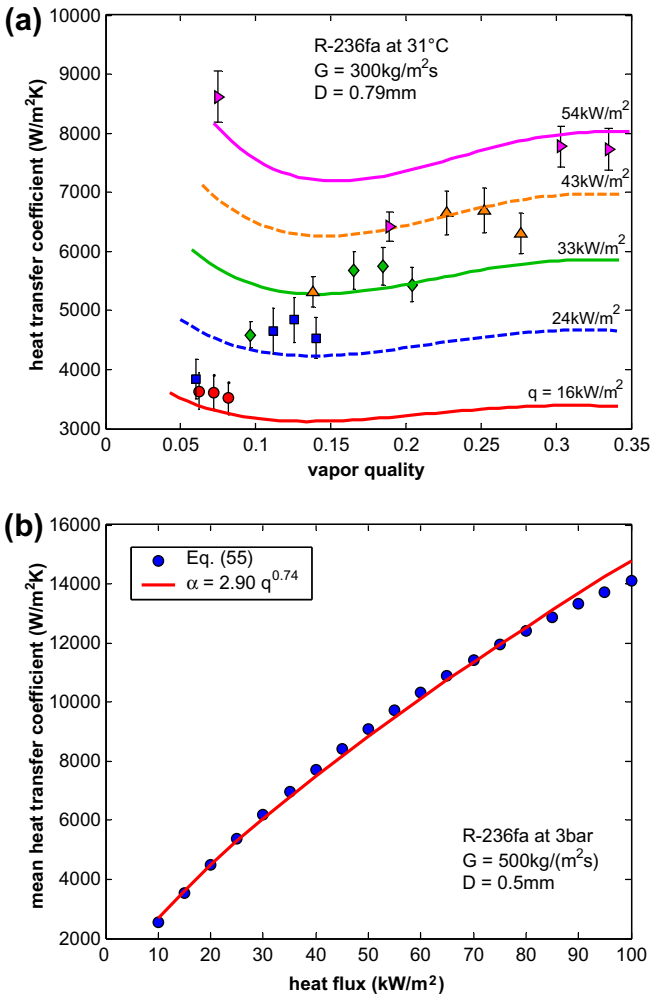

Fig. 12. (a) Experimental heat transfer coefficients versus the predictions of Eq. (59) for a flow of R-236fa at different heat fluxes (triangle-right: 54 kW/m^2, triangle: 43 kW/m^2, diamond: 33 kW/m^2, square: 24 kW/m^2, circle: 16 kW/m^2) and (b) a computed flow boiling curve for R-236fa.

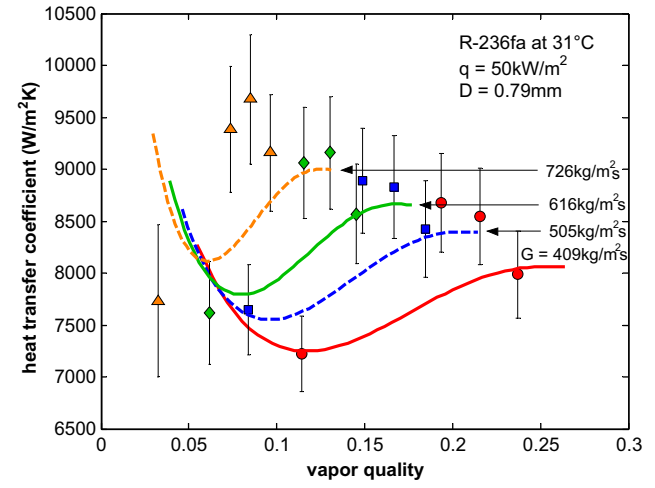

Fig. 13. Predicted versus experimental heat transfer coefficients for a flow of R-236fa at different mass velocities (triangle: 726 kg/m^2 s, diamond: 616 kg/m^2 s, square: 505 kg/m^2 s, circle: 409 kg/m^2 s).

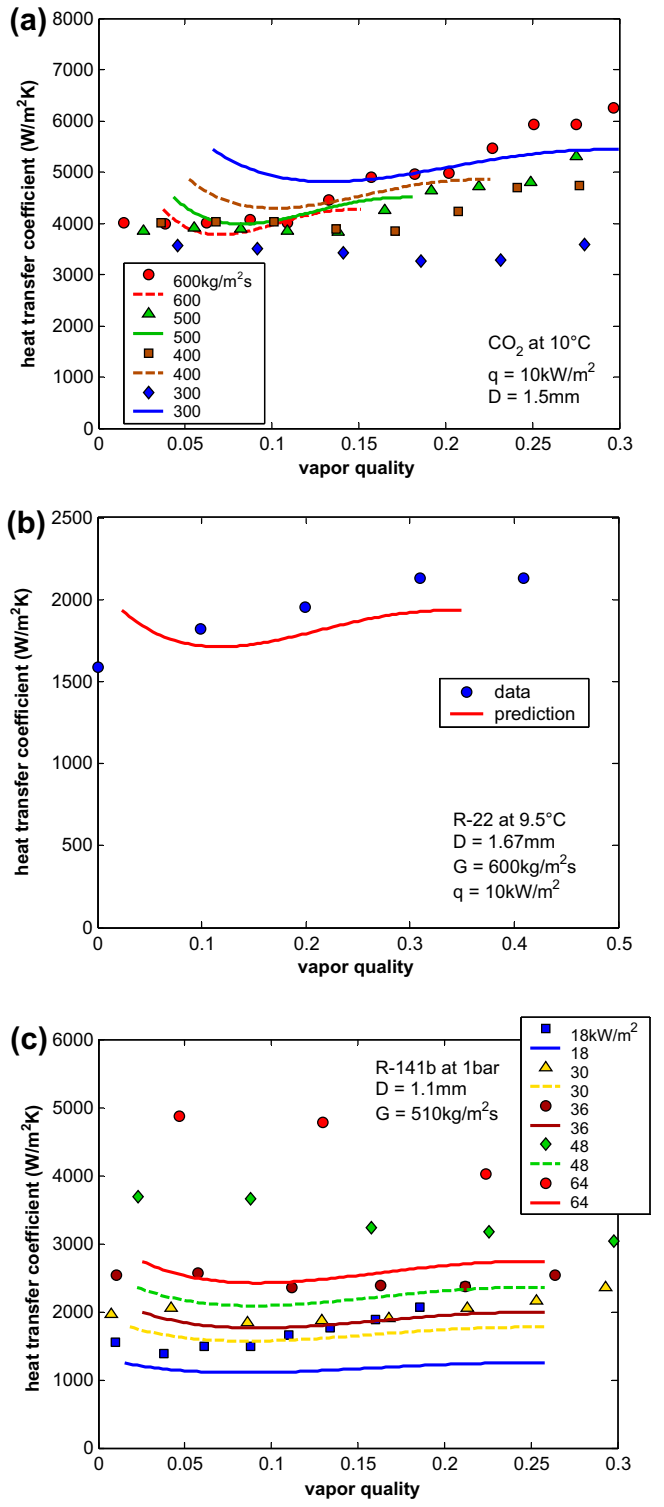

Fig. 14. Experimental heat transfer coefficients versus the prediction of Eq. (59) for (a) CO_2 at 10 °C at different mass velocities (data from Choi et al. (2007)), (b) R-22 at 9.5 °C (data from Bang and Choo (2004)), and (c) R-141b at 1 bar and at different heat fluxes (data from Lin et al. (2001)).

a film evaporation mechanism with no bubble nucleation at the heated wall.

The coalescence vapor quality, x_c, and the coalescence parameter, ψ_c, play important roles in determining the predicted behavior of the heat transfer coefficient when varying the flow mass velocity. A rise in the values of both parameters produces a decline in heat transfer. At higher G the non-dimensional shear falls (although the value of τ_i increases as approximately $G^{0.84}$), while the corresponding variation in ψ_c will depend on the change in x_c and x_a. On the other hand, Eq. (65) yields an inverse proportionality between x_c and mass velocity, with $x_c \propto 1/G^{0.78}$. The overall effect of a higher mass velocity will thus result from the combination of these parameters as in the case in Fig. 13, where the resulting rise in $\bar{\alpha}$ from a lower x_c overcomes the tendency of a lower non-dimensional shear and a higher coalescing mass flux (higher ψ_c) to reduce heat transfer.

Eq. (59) has also been confronted to independent data from other laboratories that have tested different fluids from the ones used in the current study. Fig. 14 compares the predictions to flow boiling data of CO_2, R-22 and R-141b, taken respectively from Choi et al. (2007), Bang and Choo (2004) and Lin et al. (2001). The computed values for the CO_2 and R-22 datasets show good agreement with the experimental results in both magnitude and trend with vapor quality. However, the model does not capture the increase in $\bar{\alpha}$ with mass velocity for CO_2 (Fig. 14a), which may be due to a difference in the experimental and predicted behavior of the film thickness. As was mentioned previously, the film thickness may react differently to bubble speed (and thus to G) for different values of the Bond number, and this may not be captured by the model for these particular experimental conditions. As for the R-141b data, although Eq. (59) reproduces the increase in heat transfer with heat flux, it also shows a general under-prediction of the experimental results that becomes more pronounced at the highest heat fluxes.

9. Conclusion

Eq. (53) and its extension to the entire coalescing bubble vapor quality range, given by Eq. (59), represent a micro-channel two-phase heat transfer model that includes the effects of bubble coalescence and thin film dynamics. The current approach is entirely based on the prediction of the behavior of the thin evaporating film, thus maintaining the purely convective boiling nature that was suggested by Thome et al. (2004) for micro-channels. Eq. (59) captures many of the trends in the reported experimental literature. The success in predicting the measured heat transfer coefficients within the experimental uncertainty band depends on the extent of the error due to the simplifying assumptions adopted in managing the mathematics of the problem; i.e. assuming a constant interfacial shear, setting uniform physical properties, neglecting surface tension effects, etc.

The model also clearly depends on the empirical equations developed for closure. Equations (53) and (59) are flow pattern based expressions, and thus rely on the accuracy of the adopted flow pattern map to identify the coalescing bubble flow regime boundaries, x_c and x_a. Generally, flow pattern transition equations are indicative more of a band of transition vapor qualities rather than an exact value at which the flow changes its geometry. For this reason, the predictions in the neighborhood of the transition boundaries may be subjected to higher errors than those that are well within the coalescing bubble flow mode.

As a final remark, the current approach, which has been presently developed for a constant heat flux, may potentially be extended to the time-varying heat flux case see Eqs. (11) and (27), which may be of interest in the thermal assessment of heat dissipating systems during start-up and shut-down, or highly transient operations.

References

Bang, K.H., and Choo, W.H., 2004. Flow boiling in minichannels of copper, brass and aluminum round tubes. In: Proceedings of Second International Conference on Microchannels and Minichannels, pp. 559–564.

Lin, S., Kew, P.A., Cornwell, K., 2001. Two-phase heat transfer to a refrigerant in a 1 mm diameter tube. International Journal of Refrigeration 24, 51–56.

Bertsh, S.S., Groll, E.A., Garimella, S.V., 2008. Review and comparative analysis of studies on saturated flow boiling in small channels. Nanoscale and Microscale Thermophysical Engineering 13 (3), 187–227.

Bertsch, S.S., Groll, E.A., Garimella, S.V., 2009. A composite heat transfer correlation for saturated flow boiling in small channels. International Journal of Heat and Mass Transfer 52, 2110–2118.

Choi, K., Pamitran, A.S., Oh, C., Oh, J., 2007. Boiling heat transfer of R-22, R-134a and CO_2 in horizontal smooth minichannels. International Journal of Refrigeration 30, 1336–1346.

Consolini, L., Thome, J.R., 2009. Micro-channel flow boiling heat transfer of R-134a, R-236fa and R-245fa. Microfluidics and Nanofluidics 6 (6), 731–746.

Dupont, V., Thome, J.R., Jacobi, A.M., 2004. Heat transfer model for evaporation in microchannels. Part II: comparison with the database. International Journal of Heat and Mass Transfer 47, 3387–3401.

Garimella, S., Killon, J.D., Coleman, J.W., 2003. An experimentally validated model for two-phase pressure drop in the intermittent flow regime for noncircular microchannels. Journal of Fluid Engineering 125, 887–894.

Han, Y., and Shikazono, N., 2009. Measurement of the Liquid Film Thickness in Micro Tube Slug Flow. Paper in Review.

Jacobi, A.M., Thome, J.R., 2002. Heat transfer model for evaporation of elongated bubble flows in microchannels. Journal of Heat Transfer 124, 1131–1136.

Kandlikar, S.G., Balasubramanian, P., 2004. An extension of the flow boiling correlation to transition, laminar and deep laminar flows in mini-channels and micro-channels. Heat Transfer Engineering 25 (3), 86–93.

Lazarek, G.M., Black, S.H., 1982. Evaporative heat transfer, pressure drop and critical heat flux in a small vertical tube with R-113. International Journal of Heat and Mass Transfer 25 (7), 945–960.

Moriyama, K., Inoue, A., 1996. Thickness of the liquid film formed by a growing bubble in a narrow gap between two horizontal plates. Journal of Heat Transfer 118, 132–139.

Ong, C.L., and Thome J.R., in press. Flow boiling heat transfer of R-134a, R-236fa and R-245fa in a horizontal 1.030 mm circular channel. Experimental Thermal and Fluid Science: doi:10.1016/j.expthermflusci.2009.01.002.

Revellin, R., Dupont, V., Thome, J.R., Zun, I., 2006. Characterization of diabatic two-phase flows in micro-channels: flow parameter results for R-134a in a 0.5 mm channel. International Journal of Multiphase Flow 32, 755–774.

Revellin, R., Thome, J.R., 2006. A new type of diabatic flow pattern map for boiling heat transfer in microchannels. Journal of Micromechanics Microengineering 17, 788–796.

Revellin, R., Agostini, B., Thome, J.R., 2008. Elongated bubbles in microchannels. Part II: experimental study and modeling of bubble collisions. International Journal of Multiphase Flow 34, 602–613.

Ribatski, G., Wojtan, L., Thome, J.R., 2006. An analysis of experimental data and prediction methods for flow boiling heat transfer and two-phase frictional pressure drop in micro-scale channel. Experimental Thermal and Fluid Science 31, 1–19.

Thome, J.R., Dupont, V., Jacobi, A.M., 2004. Heat transfer model for evaporation in microchannels. Part I: presentation of the model. International Journal of Heat and Mass Transfer 47, 3375–3385.

Thome, J.R., 2006. State-of-the-art overview of boiling and two-phase flows in microchannels. Heat Transfer Engineering 27, 5–19.

Tran, T.N., Wambsganss, M.W., France, D.M., 1996. Small circular- and rectangular-channel boiling with two refrigerants. International Journal of Multiphase Flow 22 (3), 485–498.

Zhang, W., Hibiki, T., Mishima, K., 2004. Correlation for flow boiling heat transfer in mini-channels. International Journal of Heat and Mass Transfer 47, 5749–5763.